Supplementary Information

Exploring P-type Transparent Conductive Materials in Conventional Binary Compounds Beyond Equilibrium Doping Limit

Haiyue Zhang,[1,3] Jinping Zhang,[2] Chunxiang Zhao,[1*] Huiwen Xiang,[4] Ke Zhao,[3*] Chengyan Liu[1,3*]

[1]College of Physics and Electronic Engineering, Nanyang Normal University, Nanyang 473061, China
[2]Faculty of Engineering, Huanghe Science and Technology College, Zhengzhou 450006, China
[3]Henan Key Laboratory of Quantum Materials and Quantum Energy, School of Quantum Information Future Technology, Henan University, Kaifeng, Henan 475001, China
[4]Center for Quantum Functional Materials and Design, and College of Physics and Optoelectronic Engineering, Zhongyuan University of Technology, Zhengzhou 450007, China
Email: zcxphys2022@nynu.edu.cn; zhaoke312@126.com; cyliu@henu.edu.cn

I. Computational methods

First-principles calculations: Electronic structure and total energy calculations for both primitive and defective systems are performed using density functional theory within the Vienna ab initio simulation package (VASP).[1, 2] The electron-core interactions are described using frozen-core projected augmented wave (PAW) approach.[3] The generalized gradient approximation (GGA) of Perdew-Burke-Ernzerhof (PBE)[4] is used for the exchange correlation functional. The Heyd-Scuseria-Ernzerhof-06 (HSE06),[5] with adjusted exchange parameters, corrects the crystal band gaps to their experimental values. Atomic structures of all primitive and defective models are relaxed until Hellmann-Feynman forces and electronic convergence less than 0.01 eV/Å and 1×10^{-4} eV, respectively. Kinetic energies cut-off for plane-wave basis functions is set to 1.5 times the maximum default value in elemental potentials. For Brillouin zone integration, k-point meshes with grid spacing of $2\pi \times 0.02$ Å^{-1} or less are used for primitive cells, and a single Γ point is used for $4 \times 4 \times 4$ supercells of selected defective models with lattice constants larger than 20 Å. The convergence tests for supercell size and kinetic energy cut-off are carefully examined. The vibrational entropy contribution to the total energy is calculated by combining VASP [S1,S2] and Phonopy software[6]. Phonon-assisted optical absorption is calculated combining Quantum Espresso[7, 8] and Yambo software,[9, 10] which can deal with basic electron/phonon properties and electron-phonon coupling. The scissor operator in Yambo is used to correct the band gaps.

Carrier effective mass: The effective masses $m^* = \hbar^2 \Big/ \frac{\partial^2 E}{\partial k^2}$ are estimated by fitting the band edges to a parabola for in a small range of wave vector along the valence and the conduction bands, where E is the band energy, k is the wave vector and $\hbar$ is the reduced Plank constant. We fully consider the electrons and holes effective masses in three directions along the high-symmetry paths, which are listed in Table S2.

Formation energy: Negative formation energy represents a good stability of compounds, defined as

$$\Delta E_{\mathrm{c}} = E(\mathrm{A}_x\mathrm{B}_y) - xE(\mathrm{A}) - yE(\mathrm{B}) \tag{S1}$$

where $E(\mathrm{A}_x\mathrm{B}_y)$, $E(\mathrm{A})$ and $E(\mathrm{B})$ is the total energy of compound $\mathrm{A}_x\mathrm{B}_y$, elemental phases A and B, respectively.

Defect formation energy: The defect formation energy reflects its formation ability, determined by the energy cost for atoms and electrons to exchange between the host and elemental and electronic reservoirs.[11, 12] Therefore, the formation energy, $\Delta H(\alpha,q)$ of defect α in charge-state q can be defined as[13, 14]

$$\Delta H(\alpha,q) = E(\alpha,q) - E(\mathrm{host}) + \sum_i n_i(\mu_i + \mu_i^0) + q(E_{\mathrm{VBM}} + E_{\mathrm{F}}) + \varepsilon_{\mathrm{ES}} \tag{S2}$$

where μ_i is the chemical potential of element i relative to its pure elemental phase μ0 i. which is limited by the formation enthalpy of compounds ΔH_{f}. E_{F} is the Fermi level relative to the host's VBM (E_{VBM}). $E(\alpha,q)$ is the total energy of a fully relaxed supercell with defect α in charge-state q, while $E(\mathrm{host})$ is the total energy of a defect-free supercell with the same size. n_i is the difference in the numbers of element i atoms between the defective system and the host. $n_i > 0$ or $n_i < 0$ indicates an atom is removed from or added to the host. $\varepsilon_{\mathrm{ES}}$ is the electrostatic correction for charged defects caused by interactions between periodic images in the finite-size supercell, determined using the SXDEFECTALIGN software.[14, 15]

Quenching treatment: Under thermodynamic equilibrium and dilute conditions, the concentration of defect α in charge-state q can be calculated as

$$n_\alpha^q = N_{\mathrm{site}} g_q \exp\left(\frac{-\Delta H_{\alpha,q}(\mu_i, E_{\mathrm{F}})}{k_{\mathrm{B}}T}\right) \tag{S3}$$

where N_{site} is the number of possible sites per volume for defect α, g_q is the degeneracy factor for possible electron occupations.[16-18] $\Delta H(\alpha,q)$ is the formation energy defined in equation (S2). Carrier concentrations are expressed by the general Fermi-Dirac statistics in equation (S4)[19, 20] which can describe degenerate semiconductors where the Fermi level is near the band edges or enters conduction or valence bands.

$$\begin{aligned} n_0 &= N_{\mathrm{C}} \frac{2}{\sqrt{\pi}} (k_B T)^{-3/2} \int_{E_{\mathrm{C}}=E_g}^{+\infty} \frac{(E - E_{\mathrm{C}})^{1/2}}{1 + \exp\left(\frac{E - E_{\mathrm{F}}}{k_{\mathrm{B}}T}\right)} d\mathrm{E}, \\ p_0 &= N_{\mathrm{V}} \frac{2}{\sqrt{\pi}} (k_B T)^{-3/2} \int_{-\infty}^{E_{\mathrm{V}}=0} \frac{(E_{\mathrm{V}} - E)^{1/2}}{1 + \exp\left(\frac{E_{\mathrm{F}} - E}{k_{\mathrm{B}}T}\right)} d\mathrm{E} \end{aligned} \tag{S4}$$

where N_{C} and N_{V} are the effective density of states of the CBM and VBM, respectively, given by

$$N_{\mathrm{C}} = \frac{2(2\pi m_{\mathrm{e}}^* k_{\mathrm{B}} T)^{3/2}}{h^3}, N_{\mathrm{V}} = \frac{2(2\pi m_{\mathrm{h}}^* k_{\mathrm{B}} T)^{3/2}}{h^3} \tag{S5}$$

where E_C and E_V are the energies of the CBM and VBM, which are set to $E_C = E_g$ and $E_V = 0$. E_g is the band gap, k_B is the Boltzmann constant, and T is the temperature. m* e and m* h are the effective masses of electrons and holes, respectively, at band edges.

The charge neutrality condition by considering the concentrations of ionized donor ($n_{D_i}^{q_i+}$) and acceptor ($n_{A_j}^{q_j-}$), respectively, can be expressed as

$$p_0 + \sum_i q_i n_{D_i}^{q_i+} = n_0 + \sum_j q_j n_{A_j}^{q_j-} \tag{S6}$$

The E_F of a defective semiconductor at given elemental chemical potentials, can be obtained by solving equation (S6) self-consistently, using equations (S2) to (S5). The defect and carrier concentrations can then be derived from equation (S3) and second terms in equation (S6), respectively.

When simulating the quenching effect, the total concentration of a defect in all possible charge states at high temperature is assumed to be unchanged. After rapid quenching to low temperature, only the concentration of defects among different charge states may change. Using a defect α with charge states 0 and q as an example,[17] the redistribution of defect concentration in charge state q is as follows

$$n'(\alpha,q) = N_{\text{site}} \frac{g_q e^{-\Delta H_f(\alpha,q)/k_B T'}}{g_q e^{-\Delta H_f(\alpha,q)/k_B T'} + g_0 e^{-\Delta H_f(\alpha,0)/k_B T'}} \tag{S7}$$

By resolving equation (S6) self-consistently, we can obtain new E_F, carrier and defect concentrations after the sample is quenched to ambient temperature T' (300 K).

II. Vibrational entropy

Table S1. Atomic number, formation energy, energy contributed by vibration entropy for Li_2Te, BeSe, MgS, CaSe and BN. The proportion of entropy energies at $T = 300$ K are very small comparing with their formation energies.

Compounds	Atom num	ΔH (eV)	$T*S$ (eV/atom)	$\Delta H+T*S$ （eV）	Proportion ($T*S/\Delta H$)
Li_2Te	3	-1.08	0.096	-0.984	8.89%
BeSe	2	-0.72	0.069	-0.651	9.58%
MgS	2	-1.40	0.082	-1.318	5.86%
CaSe	2	-1.94	0.113	-1.827	5.82%
BN	2	-1.23	0.011	-1.219	0.89%

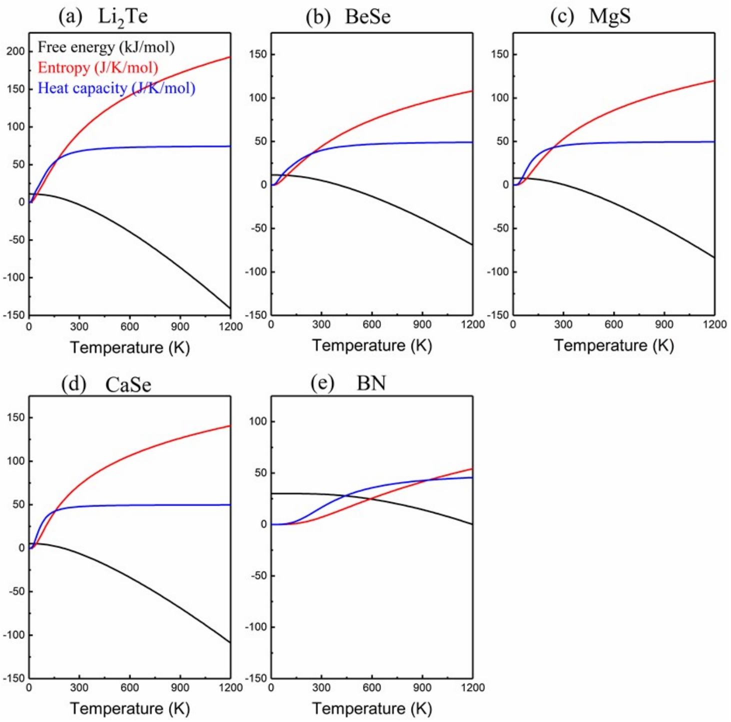

Figure S1. Free energy, entropy and heat capacity of (a) Li$_2$Te, (b) BeSe, (c) MgS, (d) CaSe and (e) BN.

III. Formation energy and relative energy of band edges

The formation energies and relative energy of band edges for binary compounds with cations from groups IA to IIIA and IB to IIB and anions from groups VA to VII, calculated by PBE functional. The formation energy is averaged per atom. Doping limit rule[21, 22] indicates that a high VBM facilitates formation of acceptor defect in ionized state, as electrons in VB can easily be excited to acceptor defect levels. Here, $E_{\mathrm{VBM}} > 2/3E$(CuI) VBM is set to ensure a good p-type dopability, as CuI is a proven efficient p-type TCM with a high VBM. The relative energy of band edges are aligned by core levels of same anion between different binary compounds. The band gap values marked by black represent they come from experiments. For materials without a determined experimental values, G_0W_0 (blue) or HSE (red) results are used. The exchange parameter of HSE is set 0.25.

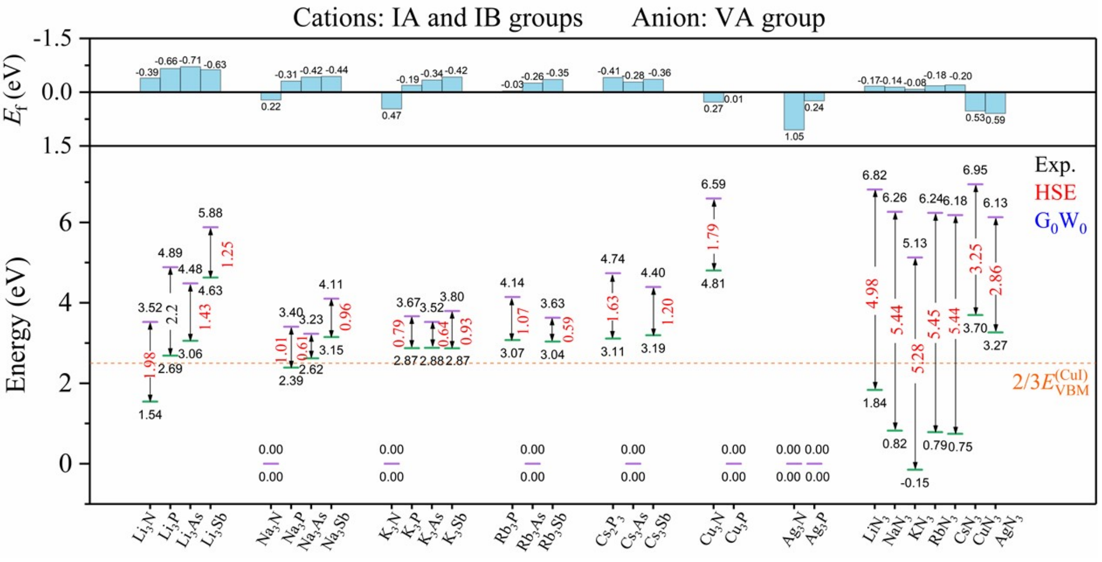

Figure S2. The formation energies and relative energies of band edges for binary compounds with cations from groups IA and IB and anions from group VA.

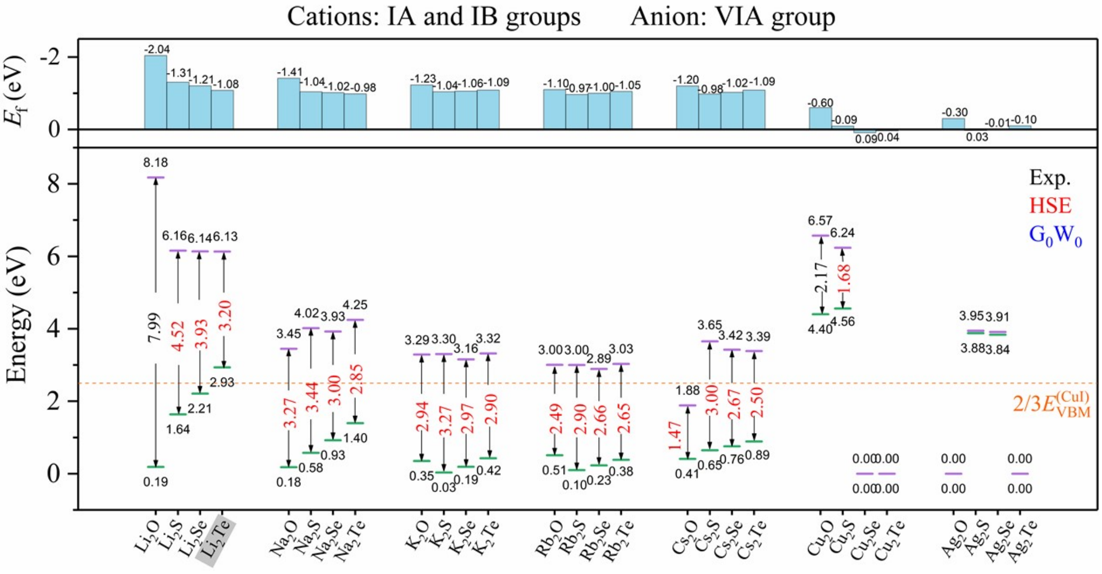

Figure S3. The formation energies and relative energies of band edges for binary compounds with cations from groups IA and IB and anions from group VIA.

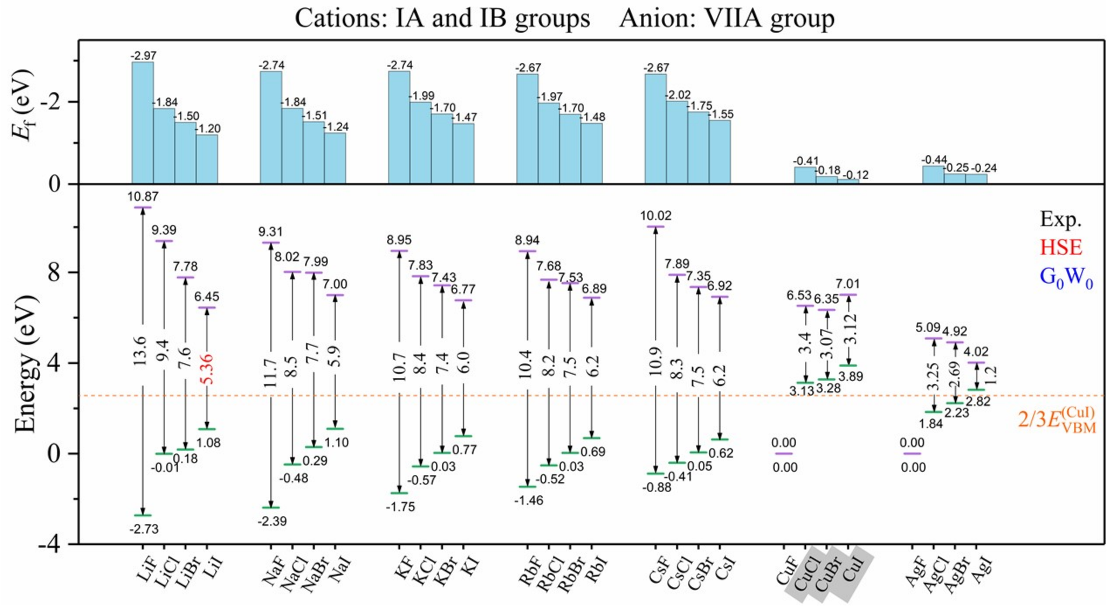

Figure S4. The formation energies and relative energies of band edges for binary compounds with cations from groups IA and IB and anions from group VIIA.

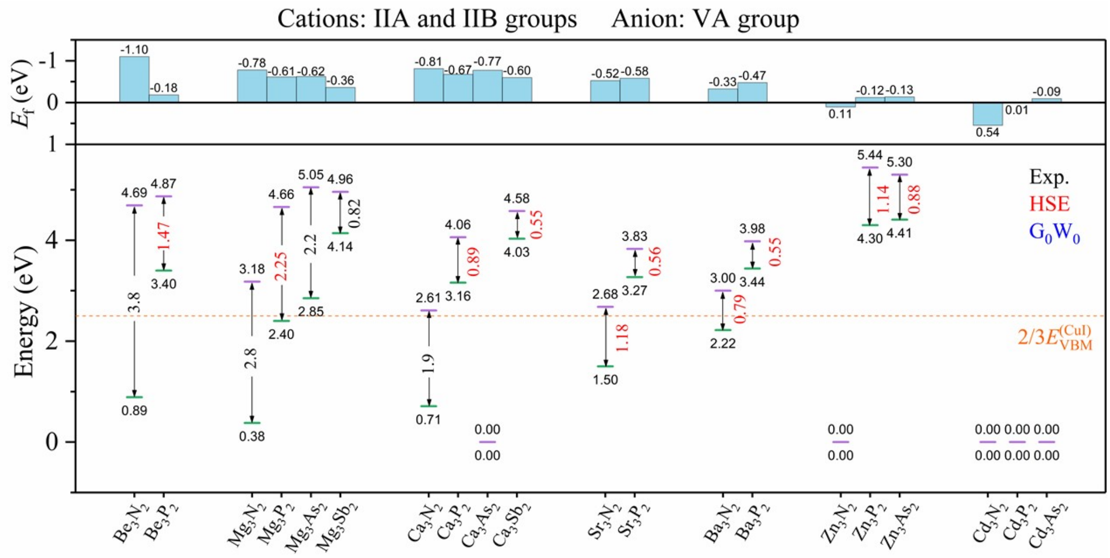

Figure S5. The formation energies and relative energies of band edges for binary compounds with cations from groups IIA and IIB and anions from group VA.

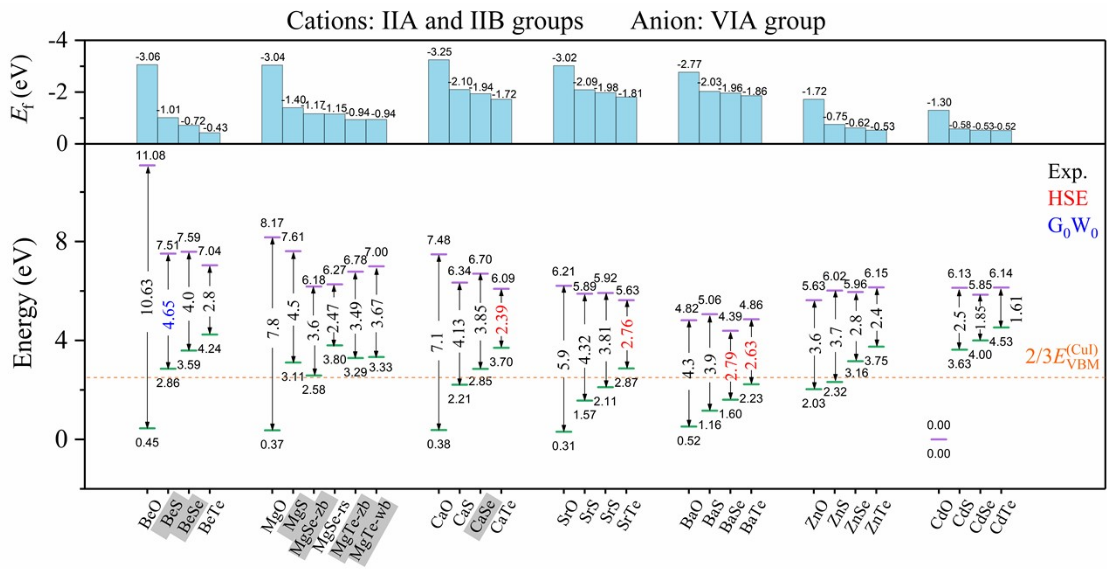

Figure S6. The formation energies and relative energies of band edges for binary compounds with cations from groups IIA and IIB and anions from group VIA.

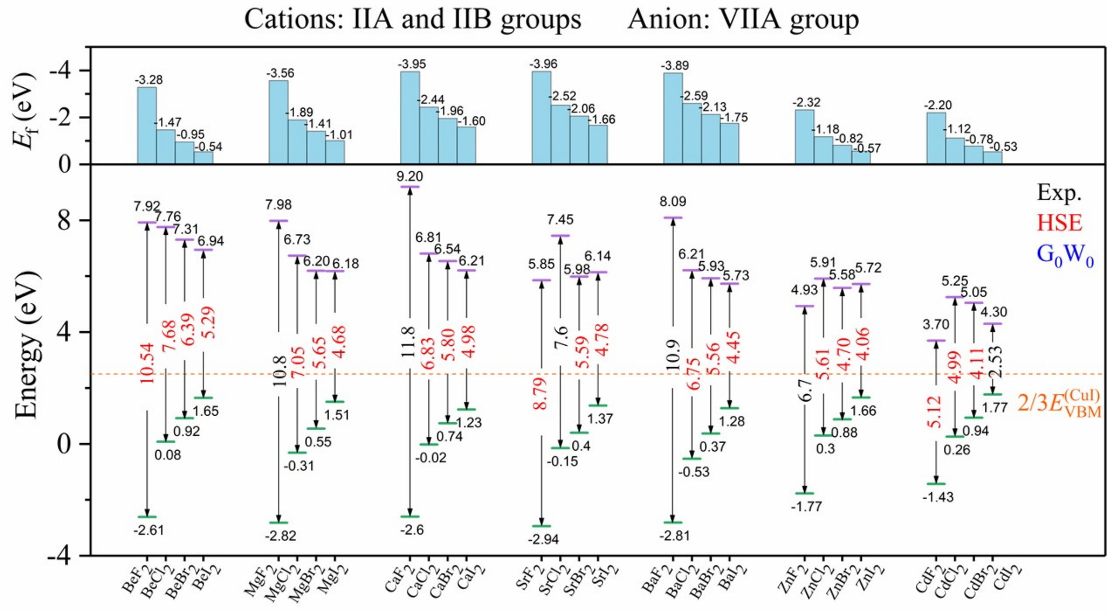

Figure S7. The formation energies and relative energies of band edges for binary compounds with cations from groups IIA and IIB and anions from group VIIA.

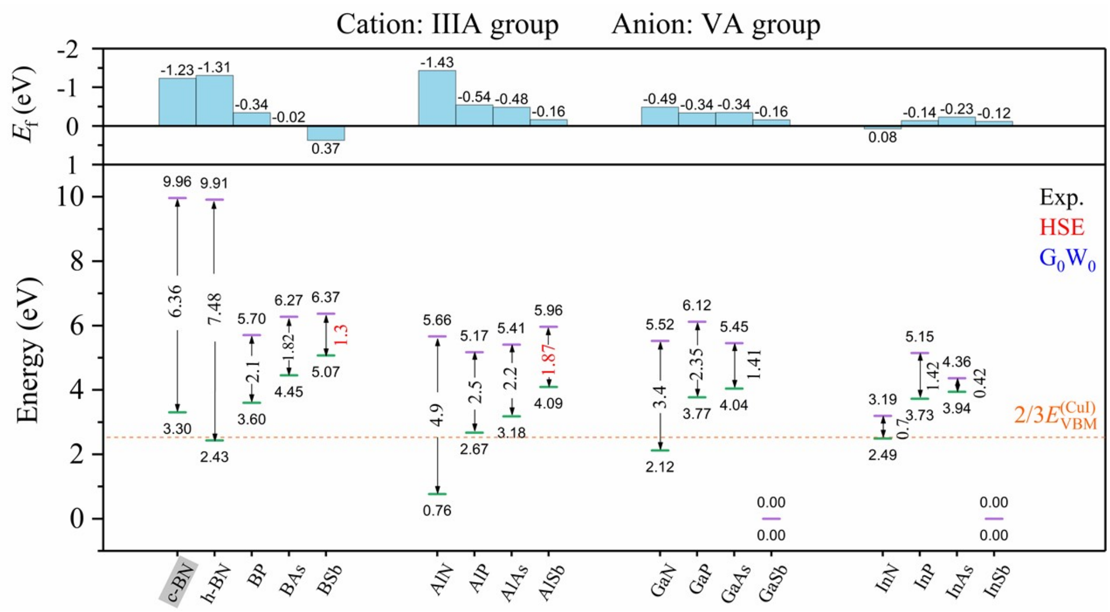

Figure S8. The formation energies and relative energies of band edges for binary compounds with cations from group IIIA and anions from group VA.

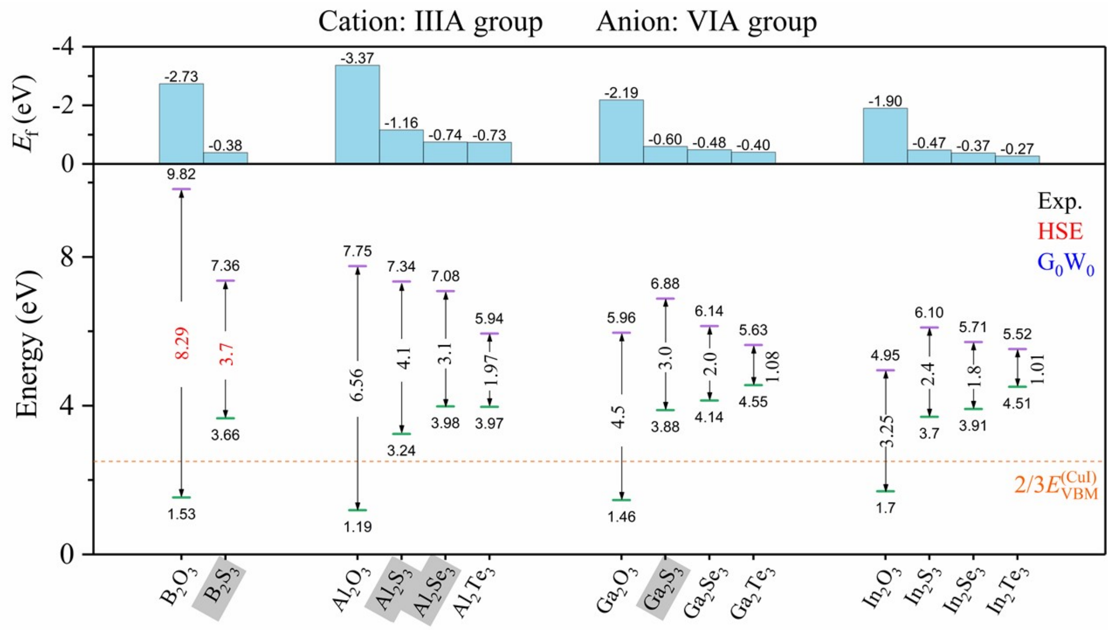

Figure S9. The formation energies and relative energies of band edges for binary compounds with cations from group IIIA and anions from group VIA.

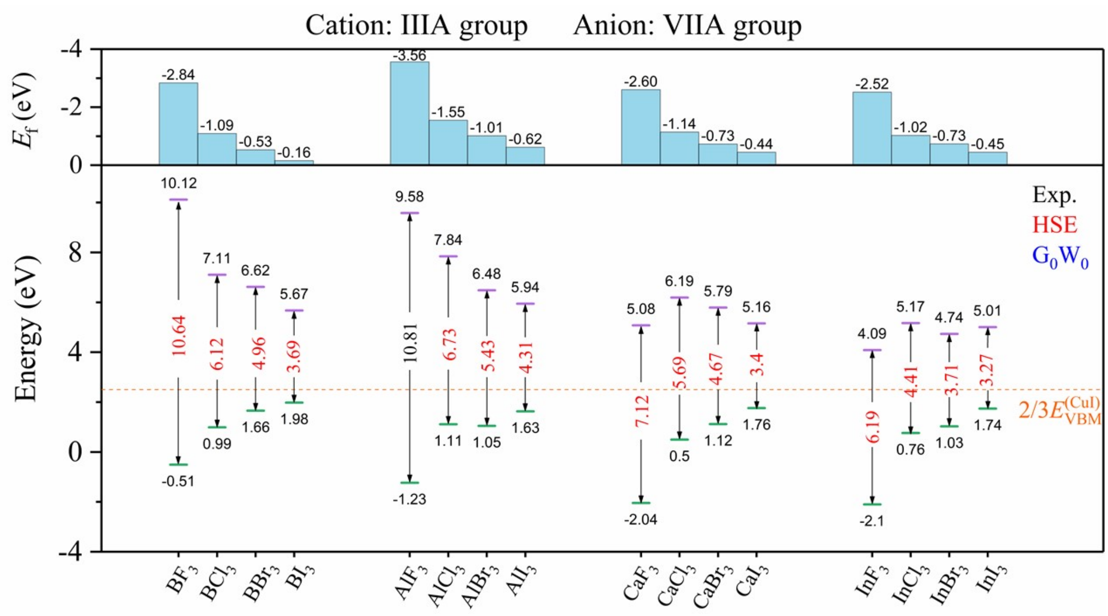

Figure S10. The formation energies and relative energies of band edges for binary compounds with cations from group IIIA and anions from group VIIA.

IV. Detailed information of the screened eight binary compounds

Table S2. The detailed information of screened eight binary compounds, including relative energies of their VBMs, formation energies, band gaps, hole effective masses, doped elements, highest hole concentrations with and without p-type doping, quenching temperatures and highest hole concentrations with and without p-type doping under high-temperature quenching.

Materials	VBM (eV)	Formation (eV)	Band gap (eV)	m_h* (light/heavy) [m_e]	Doped elements	Secondary phases	Highest hole concentration (cm^{-3})		Quenching Temperature (Melting point) (K)	Highest hole concentration (cm^{-3})		Activation Energy (eV)
							No doping	Doping		No doping quench	Doping quench	
Li_2Te	3.09	-1.08	3.2	1.49 (0.19/1.45)			10^{11}		1277 (1477)[23]	~10^{18}		0.26
BeSe	3.69	-0.72	4.0	1.09 (0.15/1.05)	Li	Li_2Se	10^{-3}	10^{3}	2100 (2300)[24]	~10^{9}	~10^{16}	0.08
MgS	2.36	-1.40	4.5	1.96 (0.19/1.92)	Na; Li	Na_2S; Li_2S	10^{-3}	$10^{0.1}$	2073 (2273)[25]	~10^{9}	~10^{16}	0.16
CaSe	2.57	-1.94	3.85	0.86 (0.22/0.78)	Na; Li; K	Na_2Se; Li_2Se; K_2Se_3	$10^{-0.1}$	10^{9}	1481 (1681)[26]	~10^{18}	~10^{20}	0.11
BN	5.39	-1.23	6.36	1.24 (0.23/1.17)	Be; Mg; Li	Be_3N_2; Mg_3BN_3; Li_3BN_2	10^{-17}	10^{5}	2800 (3000)[27]	~10^{2}	~10^{20}	0.25
BeS	3.24	-1.01	4.65	1.31 (0.19/1.26)	Li	Li_2S	10^{-9}	10^{-4}	1870 (2070)[28]	~10^{6}	~10^{7}	0.61
MgTe	3.66	-0.94	3.67	1.94 (0.19/1.90)	Li; Na	Li_2Te; $NaTe_3$	10^{-2}	$10^{-0.8}$	1100 (1300)[29]	~10^{10}	~10^{10}	0.36
Al_2S_3	3.34	-0.96	4.1	1.53 (0.55/1.29)	Mg; Be; Li	$MgAl_2S_4$; BeS; $LiAlS_2$	10^{-12}	$10^{-0.5}$	1173 (1373)[30]	~10^{4}	~10^{8}	0.59

V. Fermi levels, defect and carrier concentrations

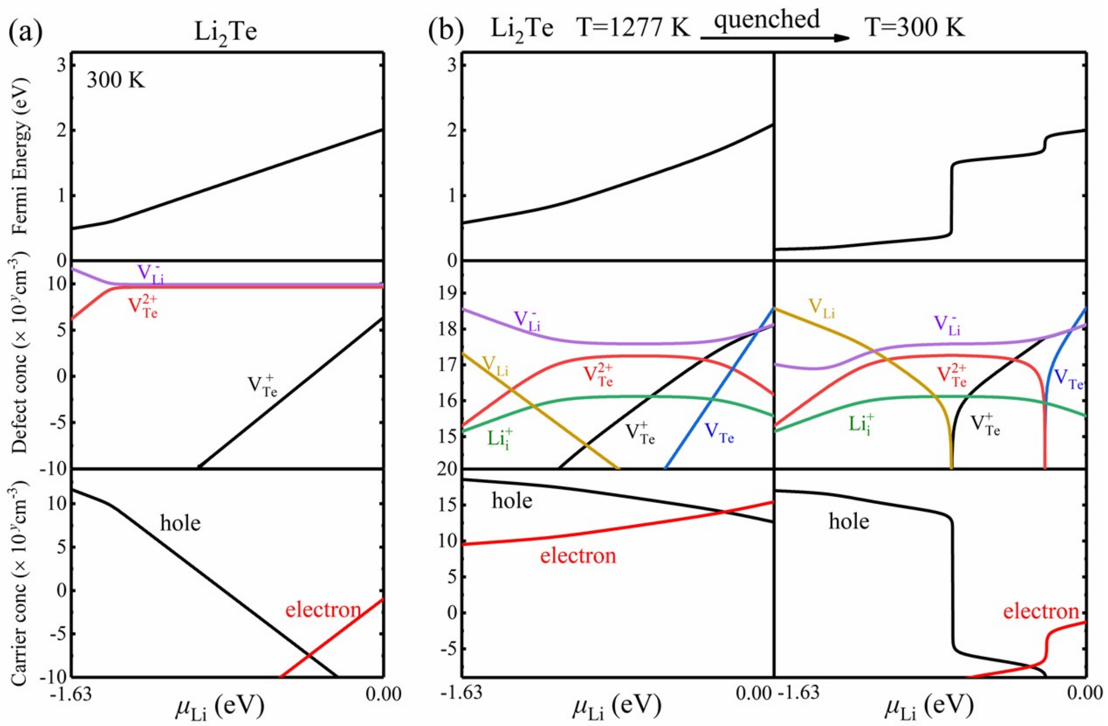

Figure S11. Fermi levels, defect and carrier concentrations as a function of Li chemical potential for Li_2Te. (a) without external doping under 300 K. (b) without external doping from 1277 K to 300 K.

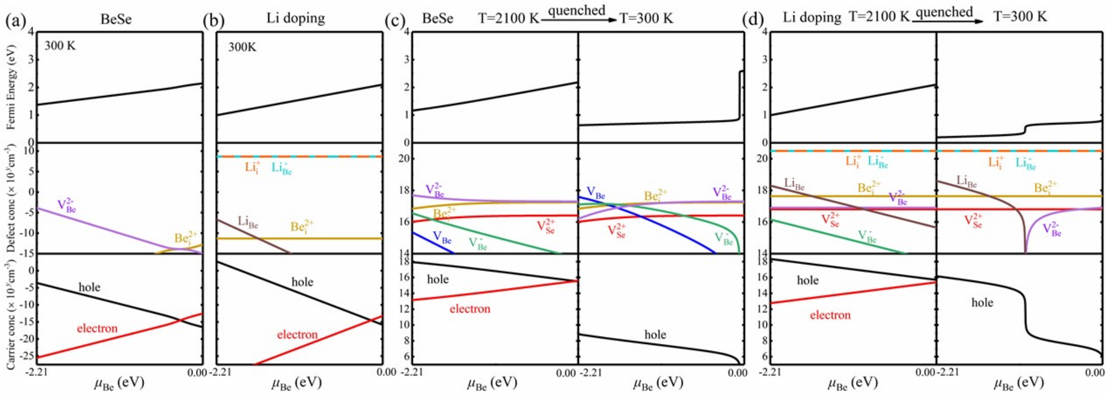

Figure S12. Fermi levels, defect and carrier concentrations as a function of Be chemical potential for BeSe. (a) and (b) without and with Li doping under 300 K, respectively. (c) and (d) without and with Li doping from 2100 K to 300 K, respectively.

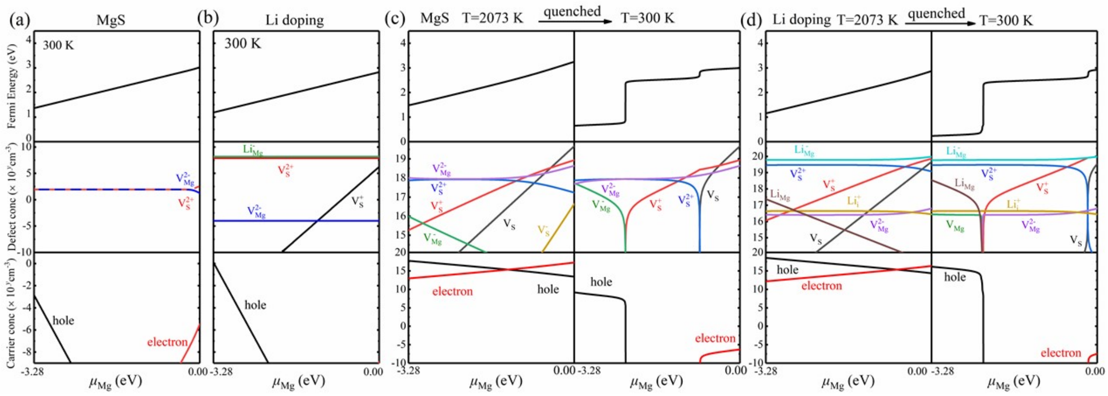

Figure S13. Fermi levels, defect and carrier concentrations as a function of Mg chemical potential for MgS. (a) and (b) without and with Li doping under 300 K, respectively. (c) and (d) without and with Li doping from 2073 K to 300 K, respectively.

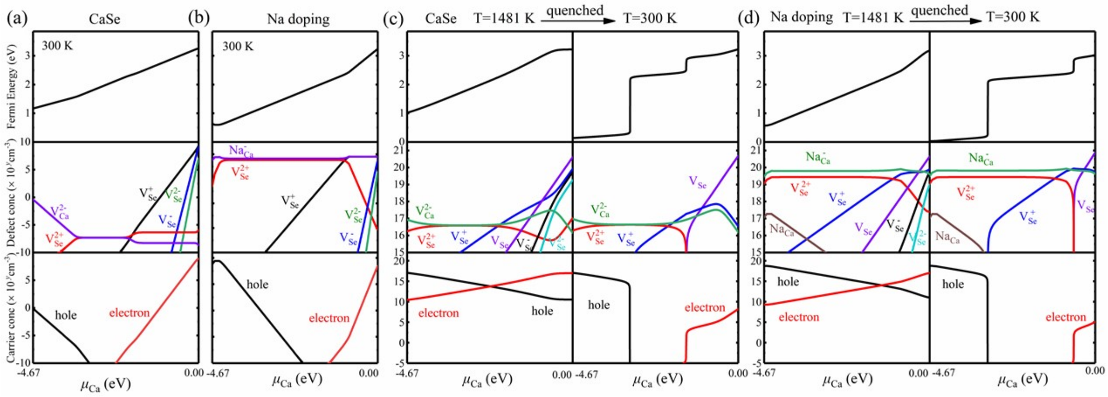

Figure S14. Fermi levels, defect and carrier concentrations as a function of Ca chemical potential for CaSe. (a) and (b) without and with Na doping under 300 K, respectively. (c) and (d) without and with Na doping from 1481 K to 300 K, respectively.

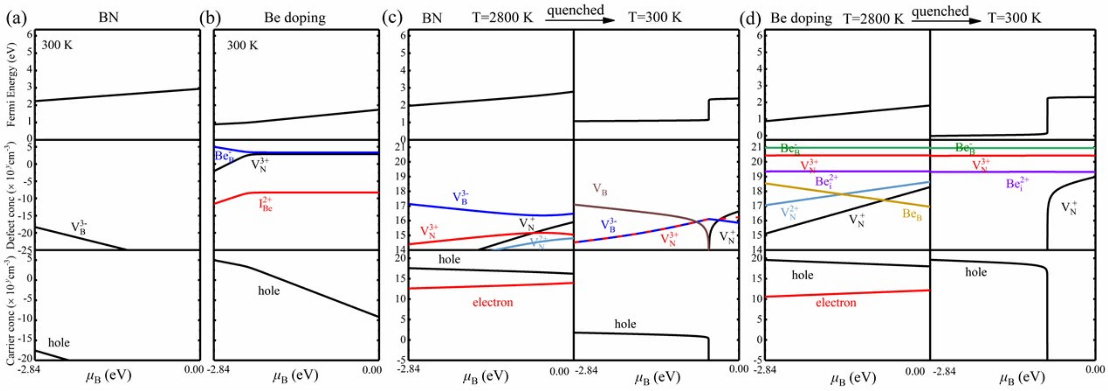

Figure S15. Fermi levels, defect and carrier concentrations as a function of B chemical potential for BN. (a) and (b) without and with Be doping under 300 K, respectively. (c) and (d) without and with Be doping from 2800 K to 300 K, respectively.

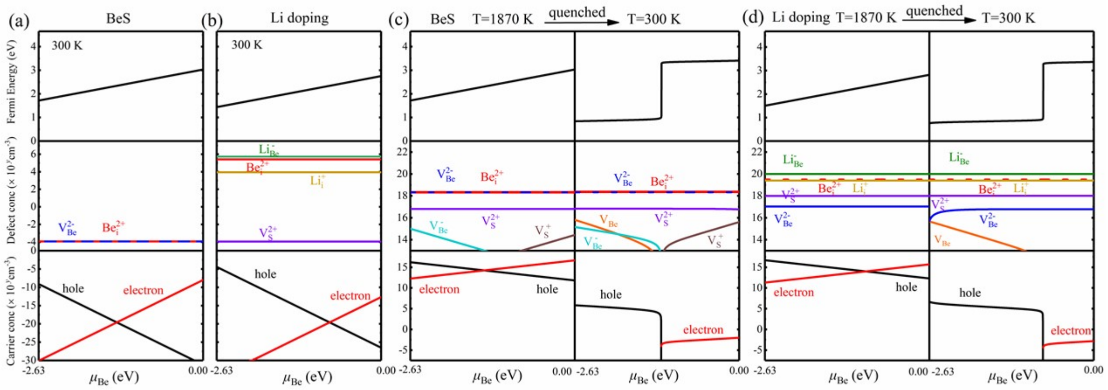

Figure S16. Fermi levels, defect and carrier concentrations as a function of Be chemical potential for BeS. (a) and (b) without and with Li doping under 300 K, respectively. (c) and (d) without and with Li doping from 1870 K to 300 K, respectively.

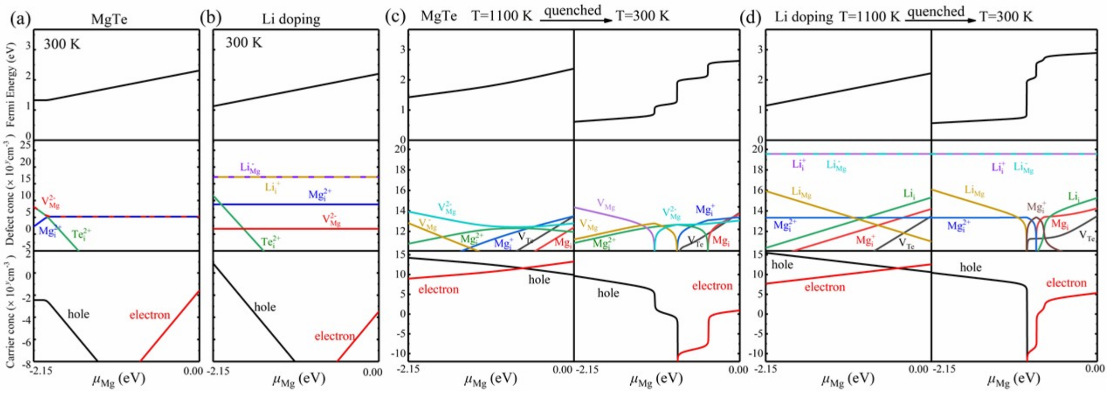

Figure S17. Fermi levels, defect and carrier concentrations as a function of Mg chemical potential for MgTe. (a) and (b) without and with Li doping under 300 K, respectively. (c) and (d) without and with Li doping from 1100 K to 300 K, respectively.

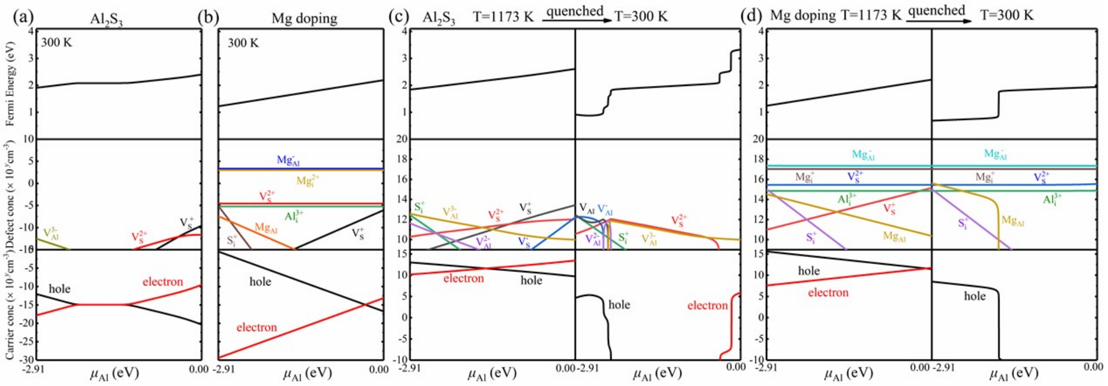

Figure S18. Fermi levels, defect and carrier concentrations as a function of Al chemical potential for Al_2S_3. (a) and (b) without and with Mg doping under 300 K, respectively. (c) and (d) without and with Mg doping from 1173 K to 300 K, respectively.

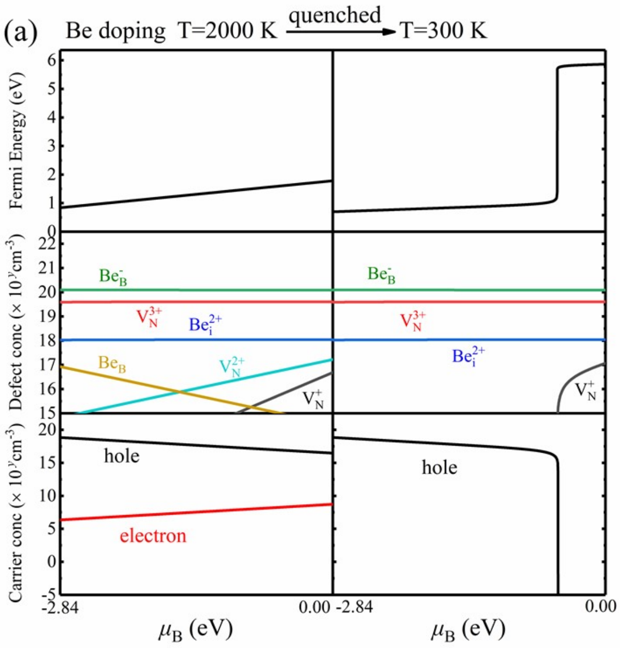

Figure S19. Fermi levels, defect and carrier concentrations as a function of B chemical potential for Be-doped BN from 2000 K to 300 K.

VI. Three-step method

As a representative, the CuI/Li_2Te heterojunction (Fig. S19a) is used to illustrate in detail how core level is applied to calibrate the band alignment. Here, we consider two compounds, *L* (CuI) and *R* (Li_2Te), with lattice constants (a_1, a_2, a_3) and (b_1, b_2, b_3), respectively, and mutually orthogonal lattice vectors. The valence band offset between the two materials can be defined as follows:

$$\Delta E_v(L/R) = \Delta E^R_{v,C*} - \Delta E^L_{v,C} + \Delta E^{L/R}_{C,C*} \tag{S8}$$

where $\Delta E^L_{v,C} = E^L_v - E^L_C$ and $\Delta E^R_{v,C*} = E^R_v - E^R_{C*}$ are the core level to VBM energy for pure *L* and *R* compounds, respectively. The three-step method as illustrated in Fig. S20b is applied to calculate the core level difference $\Delta E^{L/R}_{C,C*}$ between these two compounds. In the first step, we expand lattice a1 of compound *L* along the [100] direction, transforming it into L' with an adjusted lattice constant b_1 while retaining a_2 and a_3, resulting in a new lattice parameter set of (b_1, a_2, a_3). Then the core level difference $\Delta E^{L/L'}_{C,C'}$ between compounds *L* and L' can be derived from the electronic calculations for the L/L' superlattices oriented along the [100] direction. Similar to the first step, we expand compound L' along the [010] direction to obtain L'', adjusting the lattice constant to b_2 while maintaining b_1 and a_3, yielding the final lattice lattice parameter set of (b_1, b_2, a_3). The core level difference $\Delta E^{L'/L''}_{C',C''}$ between compounds L' and L'' can be obtained from the electronic calculation for the L'/L'' superlattices oriented along the [010] direction. In the last step, the core level difference $\Delta E^{L''/R}_{C'',C*}$

between compounds L'' and R can be obtained from the calculation for the L''/R superlattices with a matched (001) face. By transitivity, $\Delta E_{C,C*}^{L/R}$ in equation (S8) can be written as

$$\Delta E_{C,C*}^{L/R} = \Delta E_{C,C'}^{L/L'} + \Delta E_{C',C''}^{L'/L''} + \Delta E_{C'',C*}^{L''/R} \tag{S9}$$

Finally, the formula of valence band offset between compounds L and R can be expressed as

$$\Delta E_v(L/R) = \Delta E_{v,C*}^{R} - \Delta E_{v,C}^{L} + \Delta E_{C,C'}^{L/L'} + \Delta E_{C',C''}^{L'/L''} + \Delta E_{C'',C*}^{L''/R} \tag{S10}$$

To clarify the three-step method, we have added the above explanation in the part XX of Supplementary Information.

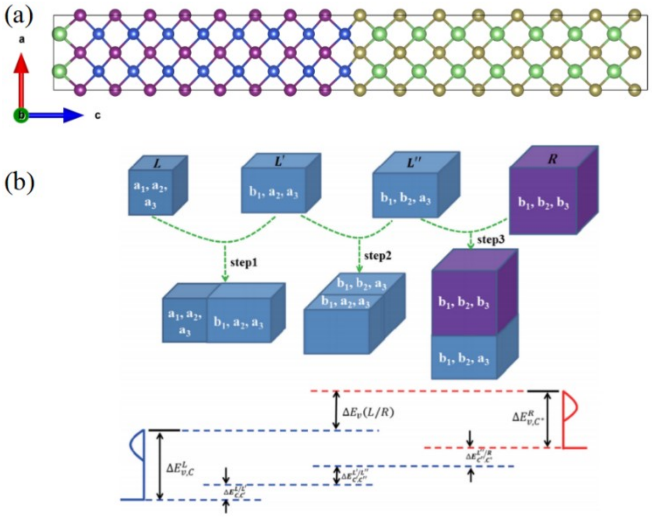

Fig. S20. (a) Atomic structure of CuI/Li_2Te superlattice. (b) Schematic illustration of the three-step method for calculating the natural band offset[31].

VII. Phonon-assisted optical absorption

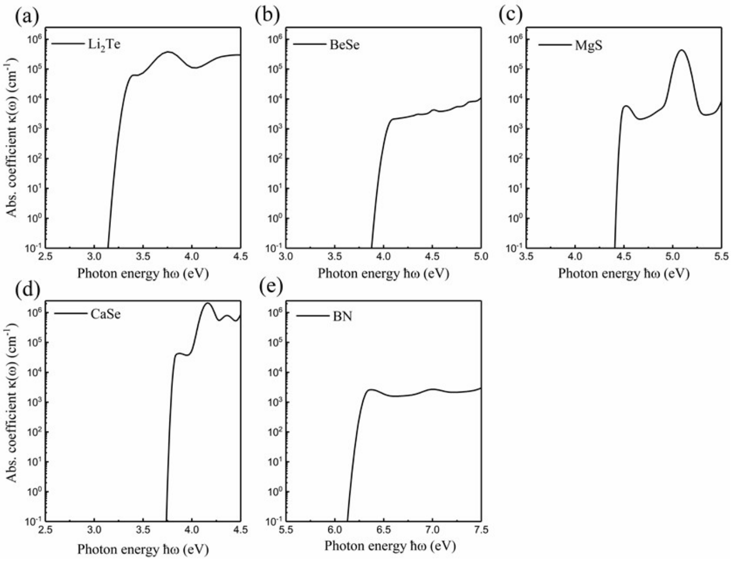

Figure S21. phonon-assisted optical absorption coefficient under 300 K. (a) Li_2Te, (b)

BeSe, (c) MgS, (d) CaSe and (e) BN.

Table S3. Comparison of key properties between our screened materials and previous reported TCMs.

Materials	E_{opt} (eV)	N_h (cm^{-3})	m_h* (m_e)	Ref.
$CuAlO_2$	3.5	1.3×10^{17}	2.39	[32, 33]
$CuScO_2$	3.3	—	3.23	[34]
$CuGaO_2$	3.6	1.7×10^{18}	2.08	[35, 36]
SnO	2.6	2.2×10^{17}	2.41	[37]
$ZnCo_2O_4$	2.26	—	—	[38]
$ZnRh_2O_4$	2.74	—	3.09	[38, 39]
$ZnIr_2O_4$	2.97	—	—	[38]
CuI	3.1	1.06×10^{18}	0.61	[40, 41]
Li_2Te	3.2	9.97×10^{16}	1.49	This work
Li-doped BeSe	4.0	1.44×10^{16}	1.09	This work
Li-doped MgS	4.5	1.40×10^{16}	1.96	This work
Na-doped CaSe	3.85	3.89×10^{18}	0.86	This work
Be-doped BN	6.36	4.55×10^{20}	1.24	This work

VII. Burstein-Moss effect on optical band gap

We have assessed the Burstein-Moss effect on optical band gap, based on the B-M shift equation[42] as follows

$\Delta E_g^{\mathrm{BM}} = \frac{h^2}{2m_{eh}^*}\left(3\pi^2 n_h\right)^{3/2}$, where $\frac{1}{m_{eh}^*} = \frac{1}{m_e^*} + \frac{1}{m_h^*}$, n_h is hole concentration, m_e^* and m_h^* are the effective masses of electron and hole. The rectified band gaps ($E'_g = E_g + \Delta E_g^{\mathrm{BM}}$) shown in Table S4 are one or two orders of magnitude smaller than the intrinsic band gaps for Li_2Te, BeSe, MgS, CaSe and BN, and can therefore be neglected.

Table S4. Intrinsic band gap (E_g), BM correction gap (ΔE_g^{BM}), rectified gap (E'_g) and the proportion of BM correction to intrinsic gap.

Compounds	Intrinsic gap E_g (eV)	BM correction gap ΔE_g^{BM} (eV)	Rectified gap E'_g (eV)	Proportion $\Delta E_g^{\mathrm{BM}} / E_g$
Li_2Te	3.2	0.027	3.227	0.844%
BeSe	4.0	0.00066	4.00066	0.016%
MgS	4.5	0.00057	4.50057	0.013%
CaSe	3.85	0.014	3.864	0.364%
BN	6.36	0.2728	6.6328	4.289%

REFERENCES

1. G. K. A and J. F. b, *Comput. Mater. Sci.*, 1996, **6**, 15-50.
2. G. Kresse and J. Furthmüller, *Phys. Rev. B*, 1996, **54**, 11169-11186.
3. G. Kresse and D. Joubert, *Phys. Rev. B*, 1999, **59**, 1758-1775.
4. J. P. Perdew, K. Burke and M. Ernzerhof, *Phys. Rev. Lett.*, 1996, **77**, 3865-3868.
5. J. Heyd, G. E. Scuseria and M. Ernzerhof, *J. Chem. Phys.*, 2003, **118**, 8207-8215.
6. A. Togo, L. Chaput, T. Tadano and I. Tanaka, *J. Phys.: Condens. Matter*, 2023, **35**, 353001.
7. F. Ren, H. Xiang, K. Zhao and C. Liu, *J. Mater. Chem. C*, 2023, **11**, 13281-13289.
8. Y.-H. Li, A. Walsh, S. Chen, W.-J. Yin, J.-H. Yang, J. Li, J. L. F. Da Silva, X. G. Gong and S.-H. Wei, *Appl. Phys. Lett.*, 2009, **94**, 212109.
9. M. Lee, Y. Youn, J. K. Jeong, Y. Kang and S. Han, *phys. status solidi (b)*, 2020, **257**, 2000218.
10. C. Yang, D. Souchay, M. Kneiß, M. Bogner, H. M. Wei, M. Lorenz, O. Oeckler, G. Benstetter, Y. Q. Fu and M. Grundmann, *Nat. Commun.*, 2017, **8**, 16076.
11. S. Chen, J.-H. Yang, X. G. Gong, A. Walsh and S.-H. Wei, *Phys. Rev. B*, 2010, **81**, 245204.
12. X.-L. Qi, Y.-S. Wu and S.-C. Zhang, *Phys. Rev. B*, 2006, **74**, 085308.
13. S.-H. Wei, *Comput. Mater. Sci.*, 2004, **30**, 337-348.
14. H. Xiang, J. Zhang, F. Ren, R. Zhu, Y. Jia and C. Liu, *Phys. Rev. Appl.*, 2023, **19**, 064036.
15. C. Freysoldt, J. Neugebauer and C. G. Van de Walle, *Phys. Rev. Lett.*, 2009, **102**, 016402.
16. J. Ma, S.-H. Wei, T. A. Gessert and K. K. Chin, *Phys. Rev. B*, 2011, **83**, 245207.
17. J.-H. Yang, J.-S. Park, J. Kang, W. Metzger, T. Barnes and S.-H. Wei, *Phys. Rev. B*, 2014, **90**, 245202.
18. H. Liang, H. Xiang, R. Zhu, C. Liu and Y. Jia, *J. Mater. Chem. A*, 2021, **9**, 14566-14575.
19. J. Auth, *Cryst. Res. Technol.*, 1986, **21**, 1548-1548.
20. S. M. Sze, and K. N. Kwok, *Phys. Semicond. Devices*, 2006, pp. 5-75.
21. S. B. Zhang, S.-H. Wei and A. Zunger, *J. Appl. Phys.*, 1998, **83**, 3192-3196.
22. S. B. Zhang, S. H. Wei and A. Zunger, *Phys. Rev. Lett.*, 2000, **84**, 1232-1235.
23. A. G. Morachevskii, *Russian J. Appl. Chem.*, 2020, **93**, 313-324.
24. s. Daoud, *Int. J. Sci. World* , 2015, **3**, 275.
25. H. Nakamura, Y. Ogawa, K. k. Gunji and A. Kasahara, *Mater. Trans.*, 1984, **25**, 692-697.
26. R. Ropp, *Encyclopedia of the Alkaline Earth Compounds*, 2013, p175.

27. H.-F. Lee, K. Esfarjani, Z. Dong, G. Xiong, A. A. Pelegri and S. D. Tse, *ACS Nano*, 2016, **10**, 10563-10572.
28. W. Zhang, C. Wang, B. Sun, J. Gu and G.-l. Ma, *Vacuum*, 2021, **186**, 110017.
29. Z. Elbahi, M. M. Zitouni, A. Gueddim and B. Bentria, *J. Eng. Exact. Sci.*, 2024, **5**, 1675-1689.
30. S. B. Bonsall and F. A. Hummel, *J. Solid State Chem.*, 1978, **25**, 379-386.
31. L. Lang, Y.-Y. Zhang, P. Xu, S. Chen, H. J. Xiang and X. G. Gong, *Phys. Rev. B*, 2015, **92**, 075102.
32. H. Kawazoe, M. Yasukawa, H. Hyodo, M. Kurita, H. Yanagi and H. Hosono, *Nature*, 1997, **389**, 939-942.
33. X.-L. Chen, B.-F. Shan, Z.-Y. Zhao, J. Zhang and Q. Liu, *Dalton trans.*, 2023.
34. R. Nagarajan, N. Duan, M. Jayaraj, J. Li, K. A. Vanaja, A. Yokochi, A. Draeseke, J. Tate and A. Sleight, *Int. J. Inorg. Mater.*, 2001, **3**, 265-270.
35. K. Ueda, T. Hase, H. Yanagi, H. Kawazoe, H. Hosono, H. Ohta, M. Orita and M. Hirano, *J. Appl. Phys.*, 2001, **89**, 1790-1793.
36. K. G. Godinho, B. J. Morgan, J. P. Allen, D. O. Scanlon and G. W. Watson, *J. Phys.: Condens. Matter*, 2011, **23**, 334201.
37. N. F. Quackenbush, J. P. Allen, D. O. Scanlon, S. Sallis, J. A. Hewlett, A. S. Nandur, B. Chen, K. E. Smith, C. Weiland, D. A. Fischer, J. C. Woicik, B. E. White, G. W. Watson and L. F. J. Piper, *Chem. Mater.*, 2013, **25**, 3114-3123.
38. M. Dekkers, G. Rijnders and D. H. A. Blank, *Appl. Phys. Lett.*, 2007, **90**, 021903.
39. A. Bouhemadou, D. Allali, K. Boudiaf, B. Qarni, S. Binomran, R. Khenata and Y. Al-Douri, *J. Alloys Compd.*, 2018, **774**.
40. D. Ahn, J. D. Song, S. S. Kang, J. Y. Lim, S. H. Yang, S. Ko, S. H. Park, S. J. Park, D. S. Kim, H. J. Chang and J. Chang, *Sci. Rep.*, 2020, **10**, 3995.
41. J. Willis, R. Claes, Q. Zhou, M. Giantomassi, G.-M. Rignanese, G. Hautier and D. O. Scanlon, *Chem. Mater.*, 2023, **35**, 8995-9006.
42. I. Hamberg, C. G. Granqvist, K. F. Berggren, B. E. Sernelius and L. Engström, *Phys. Rev. B*, 1984, **30**, 3240-3249.